



# 1 Retrieval of Solar-induced Chlorophyll Fluorescence from TanSat 2 Measurements: Comparison of SIF between TanSat and OCO-2

3 Lu Yao<sup>1, 2</sup>, Yi Liu<sup>1,3</sup>, Dongxu Yang<sup>1,3</sup>, Zhaonan Cai<sup>1</sup>, Chao Lin<sup>4</sup>, Naimeng Lu<sup>5</sup>, Daren Lyu<sup>1</sup>, Longfei  
4 Tian<sup>6</sup>, Jing Wang<sup>1</sup>, Maohua Wang<sup>3</sup>, Zengshan Yin<sup>6</sup>, Yuquan Zheng<sup>4</sup>, Sisi Wang<sup>7</sup>

5  
6 <sup>1</sup>Key Laboratory of Middle Atmosphere and Global Environment Observation, Institute of Atmospheric Physics, Chinese  
7 Academy of Sciences, No. 40, Huayan Li, Chaoyang District, Beijing 100029, China

8 <sup>2</sup>University of Chinese Academy of Sciences, No. 19A, Yuquan Lu, Shijing Shan District, Beijing 100049, China

9 <sup>3</sup>Shanghai Advanced Research Institute, Chinese Academy of Sciences, Shanghai 201210, China

10 <sup>4</sup>Changchun Institute of Optics, Fine Mechanics and Physics, Changchun 130033, China

11 <sup>5</sup>National Satellite Meteorological Center, China Meteorological Administration, Beijing 100081, China

12 <sup>6</sup>Shanghai Engineering Center for Microsatellites, Shanghai 201203, China

13 <sup>7</sup>National Remote Sensing Center of China, Beijing 100036, China

14

15

16 *Correspondence to:* Dongxu Yang (yangdx@mail.iap.ac.cn)

17 **Abstract.** Solar-induced chlorophyll fluorescence (SIF) is emitted during photosynthesis in plant leaves. It constitutes a  
18 small additional offset to reflected radiance and can be observed by sensitive instruments. The Chinese global carbon dioxide  
19 monitoring satellite (TanSat), as its mission, acquires greenhouse gas column density. The advanced technical characteristics  
20 of the hyper-spectrum grating spectrometer (ACGS) onboard TanSat enable SIF retrieval from space observations in the O<sub>2</sub>-  
21 A band. In this study, one-year SIF data was processed from Orbiting Carbon Observatory-2 (OCO-2) and TanSat using a  
22 physical-based algorithm. A comparison between the SIF retrieved from OCO-2 and its official product shows their strong  
23 linear relationship ( $R^2 > 0.85$ ) and suggests the reliability of the algorithm. The global distribution showed that the SIF  
24 retrieved from the two satellites shared the same spatial pattern for all seasons with the grided SIF difference less than 0.3 W  
25 m<sup>-2</sup> μm<sup>-1</sup> sr<sup>-1</sup>, and they also agreed with the official OCO-2 SIF product. The retrieval uncertainty of seasonal-grided TanSat  
26 SIF is less than 0.03 W m<sup>-2</sup> μm<sup>-1</sup> sr<sup>-1</sup> whereas the uncertainty of each sounding ranges from 0.1 to 0.6 W m<sup>-2</sup> μm<sup>-1</sup> sr<sup>-1</sup>. The  
27 relationship between SIF and terrestrial gross primary productivity was also estimated for data quality testing. The  
28 spatiotemporal consistency between TanSat and OCO-2 and their comparable data quality make the comprehensive usage of  
29 the two mission products possible. Data supplemented by TanSat observations are expected to contribute to the development  
30 of global SIF maps with more spatiotemporal detail, which will advance global research on vegetation photosynthesis.



## 31 1 Introduction

32 Terrestrial vegetation accounts for a large part of the ecosystem, with its photosynthesis and respiration processes playing  
33 important roles in the global carbon cycle. Incoming radiation is absorbed, reflected, and/or transmitted by plant leaves. A  
34 portion of the absorbed radiation is used by the chlorophyll in plant leaves for carbon fixation, while the rest is either  
35 dissipated as heat or re-emitted as solar-induced chlorophyll fluorescence (SIF) at longer wavelengths (Frankenberg et al.,  
36 2011a, 2014;). In contrast to the traditional remotely sensed vegetation indices obtained from some studies (Frankenberg et  
37 al., 2011b; Guanter et al., 2014; Li et al., 2018; Sun et al., 2017a; Yang et al., 2015; Zhang et al., 2014), SIF offers the  
38 potential to measure photosynthesis activity and gross primary production (GPP), due to the strong correlation between these  
39 measures (Frankenberg et al., 2011b; Guanter et al., 2012, 2014). The fluorescence emission ( $F_s$ ) adds a low-intensity  
40 radiance less than  $10 \text{ W m}^{-2} \mu\text{m}^{-1} \text{ sr}^{-1}$  and fills in the solar absorption features of the reflected spectrum (Frankenberg et al.,  
41 2011a). The filling-in effect of the solar lines (Fraunhofer lines) is the basic principle applied to measure SIF from space  
42 using the capabilities of hyperspectral observation (Frankenberg et al., 2011b; Guanter et al., 2012).

43 The first attempt at SIF research based on space-based observations was performed using images acquired by the Middle  
44 Resolution Imaging Spectrometer (MERIS) onboard the ENVIRONMENTAL SATellite (ENVISAT) (Guanter et al., 2007). This  
45 led to a new idea for conducting SIF studies on a global scale. The first global SIF map was retrieved with high-resolution  
46 spectra from the Greenhouse-gases Observing SATellite (GOSAT) (Joiner et al., 2011). After that, SIF retrievals were  
47 implemented from a variety of satellite measurements, such as those from the Global Ozone Monitoring Experiment-2  
48 (GOME-2) instruments onboard meteorological operational satellites, SCIAMACHY on board ENVISAT, and Orbiting  
49 Carbon Observatory-2 (OCO-2) (Joiner et al., 2016; Köhler et al., 2015). The TROPOspheric Monitoring Instrument  
50 (TROPOMI) on board Sentinel 5 Precursor (S-5P) provides more efficient SIF observations in terms of global coverage and  
51 new opportunities for exploring the application potential of SIF data in the terrestrial biosphere as well as in climate research  
52 (Doughty et al., 2019; Köhler et al., 2018b). Furthermore, an upcoming European Space Agency mission called  
53 FLuorescence EXplorer (FLEX), the first satellite dedicated to SIF emission observation, will launch in the middle of 2024  
54 (Drusch et al., 2017). Many studies on SIF applications have been initiated with the accumulation of SIF products in recent  
55 years. The responses of satellite-measured SIF to environmental conditions have been applied to drought dynamics  
56 monitoring and regional vegetation water stress estimation (Lee et al., 2013; Sun et al., 2015; Yoshida et al., 2015). As a  
57 proxy of photosynthesis, SIF acts as a powerful constraint parameter in estimating carbon exchange in an ecosystem between  
58 the atmosphere, ocean, and soil; as such, the analysis of the relationship between SIF and GPP has become an important  
59 research topic (Li et al., 2018; Köhler et al., 2018a; Sun et al., 2017a; Zhang et al., 2018). The strong linear relationship  
60 between them paves the way for improving terrestrial ecosystem model simulation of GPP, along with consequent  
61 improvement of global carbon flux estimation (MacBean et al., 2018; Yin et al., 2020). GPP estimations based on satellite-  
62 measured SIF have proven to be an effective method validated by in-situ flux observations (Joiner et al., 2018; Qiu et al.,  
63 2020). However, uncertainty in the factors that determine the relationship between SIF and GPP still exists and is a key



64 limitation in the application of SIF to flux estimation. Based on multi-satellite SIF products, eddy covariance flux tower  
65 observations, and ecological models, the relationship between SIF and GPP under different environmental conditions has  
66 been discussed in a number of studies to analyze the dominant factors for the growing status of different biomes, such as  
67 temperature, soil moisture, and vegetation types (Chen et al., 2020; Doughty et al., 2019; Li et al., 2020; Qiu et al., 2020; Yin  
68 et al., 2020).

69 The Chinese global carbon dioxide monitoring satellite (TanSat) was launched in December 2016. TanSat flies in a sun-  
70 synchronous orbit at approximately 700 km in height with a 16-day repeat cycle and an equator crossing time of ~1:30 p.m.  
71 local time (Cai et al., 2014; Liu et al., 2018; Yang et al., 2018). Onboard TanSat, the hyperspectral Atmospheric Carbon-  
72 dioxide Grating Spectrometer (ACGS) is designed to separately record solar backscatter spectra in three channels centered at  
73 0.76  $\mu\text{m}$  ( $\text{O}_2\text{-A}$  band), 1.61  $\mu\text{m}$  (weak  $\text{CO}_2$  absorption band), and 2.06  $\mu\text{m}$  (strong  $\text{CO}_2$  absorption band). The high spectral  
74 resolution of ~0.044 nm and a signal-to-noise ratio of ~360 in the  $\text{O}_2\text{-A}$  band makes it possible to obtain SIF from space  
75 measurements, with a spatial resolution of 2 km  $\times$  2 km in nadir mode (Liu et al., 2018).

76 Many Optimal Estimation Method (OEM) full physics retrieval algorithms have been developed and applied for GOSAT,  
77 OCO-2, and TanSat XCO<sub>2</sub> retrievals (Boesche et al., 2009; Butz et al., 2009, 2011; O'Dell et al., 2012; Reuter et al., 2010;  
78 Yang et al., 2015b; Yoshida et al., 2011, 2013). The Institute of Atmospheric Physics Carbon Dioxide Retrieval Algorithm  
79 for Satellite Remote Sensing (IAPCAS) algorithm has been applied for TanSat retrieval (Yang et al., 2018; Yang et al., 2021)  
80 and was also previously tested on GOSAT and OCO-2 missions (Yang et al., 2015b). However, the fluorescence feature  
81 causes substantial biases when retrieving surface pressure and scattering parameters from the  $\text{O}_2\text{-A}$  band, and the associated  
82 errors propagate into the XCO<sub>2</sub> retrievals. In previous XCO<sub>2</sub> retrieval, the surface emissions were well modeled as a  
83 continuum zero offset of the  $\text{O}_2\text{-A}$  band to reduce errors (Frankenberg et al., 2011a, 2012; Butz et al., 2009, 2010; Joiner et  
84 al., 2012).

85 Various approaches have been used to infer SIF from satellite measurements (Frankenberg et al., 2011b, 2014; Guanter et al.,  
86 2007, 2012, 2015; Joiner et al., 2011, 2013, 2016; Köhler et al., 2015, 2018b). The SIF signal induces a filling-in effect of  
87 solar lines, which can be used for SIF retrieval, as the fractional depth of solar Fraunhofer lines does not change during  
88 radiation transmission in the atmosphere. To recognize the filling-in features by SIF, high-resolution spectra and an  
89 instrument spectral response function (ISRF) are required to describe subtle changes in the spectral absorption lines. With  
90 the detailed spectrum features, a method was developed based on solar line fitting and the Beer-Lambertian law. This  
91 method is robust and accurate when the spectrum is out of the influence of telluric absorptions, even in the presence of  
92 aerosols (Frankenberg et al., 2011a; Joiner et al., 2011); in the current study, this method was applied to develop the  
93 IAPCAS/SIF algorithm. Another SIF retrieval method is the data-driven algorithm based on the singular value  
94 decomposition (SVD) technique (Guanter et al., 2012), which has been broadly applied in GOSAT and TROPOMI SIF  
95 retrieval. In the data-driven method, the spectrum is represented as a linear combination of the SIF signal and several  
96 singular vectors that are trained from non-fluorescent scenes by SVD; thus, the SIF signal can be obtained with linear least-  
97 squares fitting (Du et al., 2018; Guanter et al., 2012). In a previous study, a preliminary comparison between the TanSat SIF

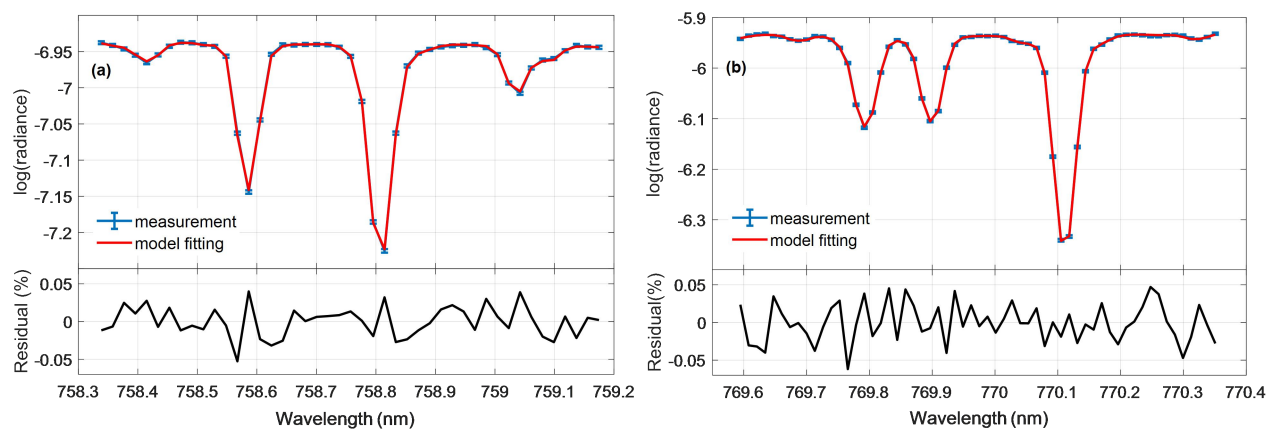


98 products retrieved by IAPCAS/SIF algorithm and the SVD data-driven method was performed to test the IAPCAS/SIF  
 99 algorithm and for further algorithm optimization (Yao et al., 2021). In this study, we introduce TanSat SIF retrieval using the  
 100 IAPCAS/SIF algorithm and the comparison of SIF products between TanSat and OCO-2. To avoid duplication of  
 101 information, we use the SIF product at 757nm as the example in the analysis.

## 102 2 Data and retrieval algorithm

### 103 2.1 Retrieval Principle and Method

104 We used TanSat version 2 Level 1B (L1B) nadir-mode earth observation data in the retrieval process. The measurements  
 105 covered the period from March 2017 to February 2018. Polarized radiance in the O<sub>2</sub>-A band with a spectral resolution of  
 106 0.044 nm was provided in the L1B data, and two micro-windows near 757 nm (758.3-759.2 nm) and 771 nm (769.6-770.3  
 107 nm) were chosen to retrieve the top-of-atmosphere (TOA) SIF while avoiding the contamination from strong lines of  
 108 atmospheric gas absorption. The retrieval was independent for each micro-window as shown in Figure 1.



109  
 110 **Figure 1: The fitted spectra and residuals for the (a) 757 nm and (b) 771 nm micro-windows of TanSat measurement. The error**  
 111 **bar of the measured spectra depicts the estimated precision of each TanSat sounding.**

112  
 113 Filling-in on solar lines by chlorophyll fluorescence in the O<sub>2</sub>-A band can be detected in the hyperspectral measurements  
 114 from TanSat. This effect on spectral radiance is different from the impact of atmospheric and surface processes, e.g.,  
 115 scattering and absorption. For example, scattering by aerosols and clouds does not change the relative depth of clear solar  
 116 lines, unlike the SIF emission signal. We applied the differential optical absorption spectroscopy (DOAS) technique to  
 117 IAPCAS/SIF algorithm for TanSat measurement.

118 The TOA spectral radiance ( $L_{TOA}^\lambda$ ) at wavelength  $\lambda$  can be represented as follows:

$$119 L_{TOA}^\lambda = I_t^\lambda \cdot \mu_0 \cdot \left( \rho_0^\lambda + \frac{\rho_s^\lambda \cdot T_d^\lambda \cdot T_t^\lambda}{\pi} \right) + F_{TOA}^\lambda \quad (1)$$



120 where  $I_t^\lambda$  is the incident solar irradiance at the TOA,  $\mu_0$  is the cosine of the solar zenith angle (SZA),  $\rho_0^\lambda$  is atmospheric path  
121 reflectance,  $\rho_s^\lambda$  is surface reflectance, and  $T_\downarrow^\lambda$  and  $T_\uparrow^\lambda$  are the total atmospheric transmittances along the light-path in the  
122 downstream and upstream directions, respectively.  $F_{TOA}^\lambda$  is the SIF radiance at TOA.

123 The first term on the right of Eq. (1) represents the transmission process of solar radiance. In the micro-windows used in SIF  
124 retrieval, gas absorption is very weak and smooth, and hence, the atmosphere term  $\mu_0 \cdot (\rho_0^\lambda + \frac{\rho_s^\lambda \cdot T_\downarrow^\lambda \cdot T_\uparrow^\lambda}{\pi})$  can be simplified to a  
125 low-order polynomial that varies with  $\lambda$  (Joiner et al., 2013; Sun et al., 2018); this is always valid as long as the spectrum  
126 fitting range is out of sharp atmospheric absorptions. In the retrieval, the spectral radiance measurement was converted to  
127 logarithmic space by the instrument and the radiative transfer process  $f(F_s^{rel}, \mathbf{a})$  was represented as follows:

$$128 \quad f(F_s^{rel}, \mathbf{a}) = \log(\langle I_t + F_s^{rel} \rangle) + \sum_{i=0}^n a_i \cdot \lambda^i \quad (2)$$

129 where  $\langle \rangle$  denote the convolution with the ISRF from line-by-line spectra. The polynomial coefficient  $\mathbf{a}$  determines the  
130 wavelength dependence polynomial for the atmosphere term; in the retrieval, we used a second-order polynomial ( $n = 2$ ).  
131 The radiance is normalized to the continuum level; hence,  $I_t$  is a normalized disk-integrated solar transmission model, and  
132  $F_s^{rel}$  is the normalized relative SIF. In the micro-window, SIF was regarded as a constant signal due to its small changes.

133 Although the atmospheric gas absorption was very weak in the micro-window, the weak absorption and the far-wing effects  
134 ( $O_2$  lines) can still change spectral features, which induces errors in spectrum fitting. Therefore, we used the European  
135 Centre for Medium-Range Weather Forecasts (ECMWF) interim surface pressure ( $0.75^\circ \times 0.75^\circ$ ) to estimate  $O_2$  absorption  
136 firstly and modified the absorption feature by a scale factor to reduce the error induced by the uncertainty in surface pressure.  
137 The scale factor is obtained simultaneously in SIF retrieval. As described by Yang (2020), there is also a continuum feature  
138 in TanSat L1B data that needs to be considered for the high-quality fitting of the  $O_2$ -A band. However, in this study, this  
139 continuum feature was not corrected, as the impact of such a smooth continuum variation in the micro-window is weak and  
140 the polynomial continuum model is capable of compensating for most of this effect.

141 The state vector list in the retrieval includes the relative SIF signal  $F_s^{rel}$ , a wavenumber shift, the scale of  $O_2$  column  
142 absorption for surface pressure correction, and coefficients of the polynomial. The continuum level radiance  $I_{cont}$  within the  
143 fitting window is calculated using the side radiance in the micro-window and is then used for the actual SIF signal  
144 calculation thus:  $F = F_s^{rel} \cdot I_{cont}$ .

145 In the IAPCAS/SIF algorithm, we used an OEM for state vector optimization in the retrieval process. Considering that the  
146 complexity of SIF retrieval is lower than that of  $XCO_2$  retrieval, the Gauss-Newton method was applied in inversion  
147 iteratively to find the optimal solution.

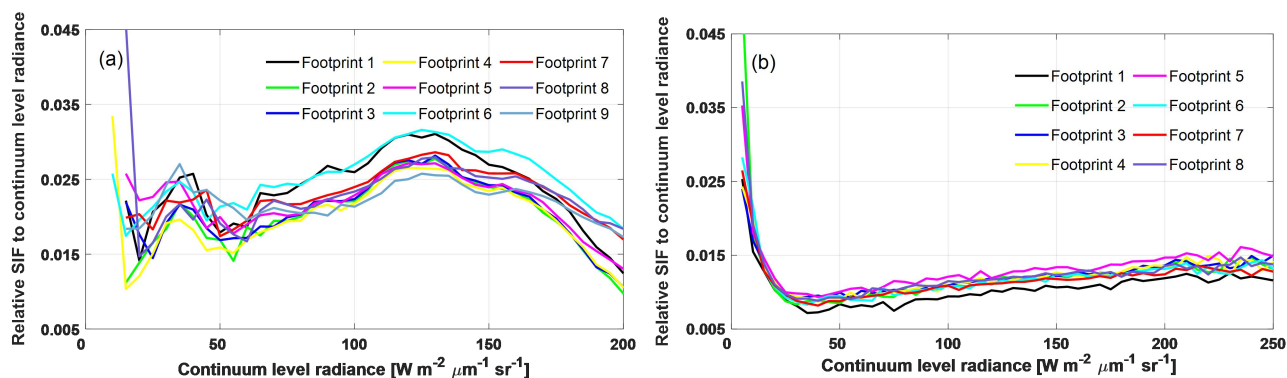
## 148 2.2 Bias Corrections

149 A significant error remains in the raw SIF retrieval output if no bias correction is performed; similar results have been  
150 reported in GOSAT and OCO-2 SIF retrieval studies (Frankenberg et al., 2011a, 2011b; Sun et al., 2018). This is because the  
151 SIF signal is weak (e.g., typically  $\sim 1$ -2% of the continuum level radiance), which means that even a small issue in the



152 measurement, such as a zero-offset caused by radiometric calibration error, could induce significant bias. Unfortunately, the  
 153 lack of knowledge on in-flight instrument performance makes it difficult to perform a direct systematic bias correction in the  
 154 measured spectrum. In the retrieval, a continuum level radiance bin fit was used to estimate the bias. The bins have a  
 155 continuum level radiance interval of  $5 \text{ W m}^{-2} \mu\text{m}^{-1} \text{ sr}^{-1}$ . In each bin, the mean bias was estimated using all non-fluorescence  
 156 measurements, and a piecewise linear function was built from the mean bias of each continuum level radiance interval.  
 157 The non-fluorescence soundings that were used in the bias estimation were based on the dataset “sounding\_landCover” in  
 158 TanSat L1B data. This dataset depends on the MODIS land cover product and provides a scheme consisting of 17 land cover  
 159 classifications defined by the International Geosphere-Biosphere Programme. These retrieved measurements marked as  
 160 “snow and ice,” “barren,” and “sparsely vegetated” were chosen to estimate the bias. Calibrations compensated for most of  
 161 the instrument degradations, but this alone was not perfect. To reduce the impact from the remaining minor discrepancies,  
 162 we built the bias correction function daily to obtain bias for each sounding via interpolation of the continuum level radiance  
 163 (Sun et al., 2017b, 2018).

164 The bias curves shown in Figure 2 differ significantly between TanSat and OCO-2. This is mostly due to the differences in  
 165 instrument performance and radiometric calibration. In general, the TanSat bias curves exhibited two peaks at radiance levels  
 166 of approximately 40 and  $125 \text{ W m}^{-2} \mu\text{m}^{-1} \text{ sr}^{-1}$ , separately, and most biases were larger than 0.015. For OCO-2, the curves  
 167 dropped sharply at low radiance levels, reaching the valley at a radiance level of approximately  $40 \text{ W m}^{-2} \mu\text{m}^{-1} \text{ sr}^{-1}$ , and then  
 168 increased slowly with the radiance level.



169  
 170 **Figure 2: Variations in the bias correction curves of continuum level radiance from (a) TanSat on July 7, 2017, and (b) Orbiting**  
 171 **Carbon Observatory-2 (OCO-2) on June 16, 2017 for each footprint.**

### 172 2.3 Data Quality Controls

173 Only data that passed quality control were used in further applications. There were two data quality control processes for the  
 174 SIF products: pre-screening and post-screening. Pre-screening focused mainly on cloud screening; only cloud-free  
 175 measurements were used in SIF retrieval. A surface pressure difference (SPD), defined as:

$$176 \Delta P_0 = |P_{\text{retrieval}} - P_{\text{ECMWF}}| \quad (3)$$

177 was used to evaluate cloud contamination along with a chi-square test



$$\chi^2 = \sum \frac{(y_{sim} - y_{obs})^2}{y_{noise}^2} \quad (4)$$

179 where  $y_{sim}$ ,  $y_{obs}$ , and  $y_{noise}$  represent the model fitting spectrum, observation spectrum, and spectrum noise, respectively.  
180  $P_{retrieval}$  is the apparent surface pressure obtained from O<sub>2</sub>-A band surface pressure retrieval, assuming a single scattering  
181 atmosphere.  $P_{ECMWF}$  is the ECMWF interim (0.75° × 0.75°) surface pressure. A “cloud-free” measurement was required to  
182 simultaneously satisfy an SPD of less than 20 hPa and a  $\chi^2$  value of less than 80. Here, post-screening was applied to filter  
183 out “bad” retrievals; this screening process involved the following steps: (1) SIF retrievals with reduced  $\chi^2$  ( $\chi_{red}^2$ ) values  
184 ranging from 0.7 to 1.3 were considered “good” fitting, (2) continuum level radiance between 15 and 200 W m<sup>-2</sup> μm<sup>-1</sup> sr<sup>-1</sup>  
185 was screened out to avoid scenes too bright or too dark, and (3) soundings with the SZA higher than 60° were also filtered  
186 out.

#### 187 2.4 IAPCAS versus IMAP-DOAS OCO-2 SIF Retrieval

188 Before applied to TanSat retrievals, we tested the IAPCAS/SIF algorithm on the OCO-2 L1B data firstly  
189 (OCO2\_L1B\_Science.8r) and then compared the retrieval results with the OCO-2 L2 Lite SIF product (OCO2\_Level  
190 2\_Lite\_SIF.8r) retrieved by the Iterative Maximum A Posteriori-Differential Optical Absorption Spectroscopy (IMAP-  
191 DOAS) algorithm.

192 Table 1 displays the relationship of OCO-2 SIF values between the IAPCAS/SIF and IMAP-DOAS at 757 nm micro-  
193 window for each month. Overall, the two SIF products were in good agreement. The linear fitting of the two SIF products  
194 suggests that they are highly correlated, as indicated by the strong linear relationship with R<sup>2</sup> mostly larger than 0.85 and the  
195 root mean square error (RMSE) of about 0.2 W m<sup>-2</sup> μm<sup>-1</sup> sr<sup>-1</sup>. Good consistency between the two SIF products implies the  
196 reliability of the IAPCAS/SIF algorithm; thus, it was further applied for TanSat SIF retrieval. However, there was still a  
197 small bias remained in the comparisons, which was due, most likely, to the impact of differences in the bias correction  
198 method, retrieval algorithm, and fitting window.

199 **Table 1:** Summary of the relationship between the Institute of Atmospheric Physics Carbon Dioxide Retrieval Algorithm for  
200 Satellite Remote Sensing (IAPCAS) OCO-2 and Iterative Maximum A Posteriori-Differential Optical Absorption Spectroscopy  
201 (IMAP-DOAS) OCO-2 solar-induced chlorophyll fluorescence (SIF) products at 757nm micro-window.

month	Number of soundings	R <sup>2</sup>	RMSE/ W m <sup>-2</sup> μm <sup>-1</sup> sr <sup>-1</sup>
2017/03	1097277	0.86	0.18
2017/04	1119464	0.87	0.19
2017/05	1054235	0.88	0.19
2017/06	1014848	0.90	0.19
2017/07	965309	0.91	0.19
2017/09	211219	0.81	0.23
2017/10	473359	0.88	0.17
2017/11	579009	0.85	0.19



2017/12	645134	0.88	0.16
2018/01	788655	0.88	0.17
2018/02*	629995	0.87	0.18

202 \* Due to the lack of OCO-2 measurements in August 2017, the comparison is only performed for 11 months.

## 203 3 Results and Discussion

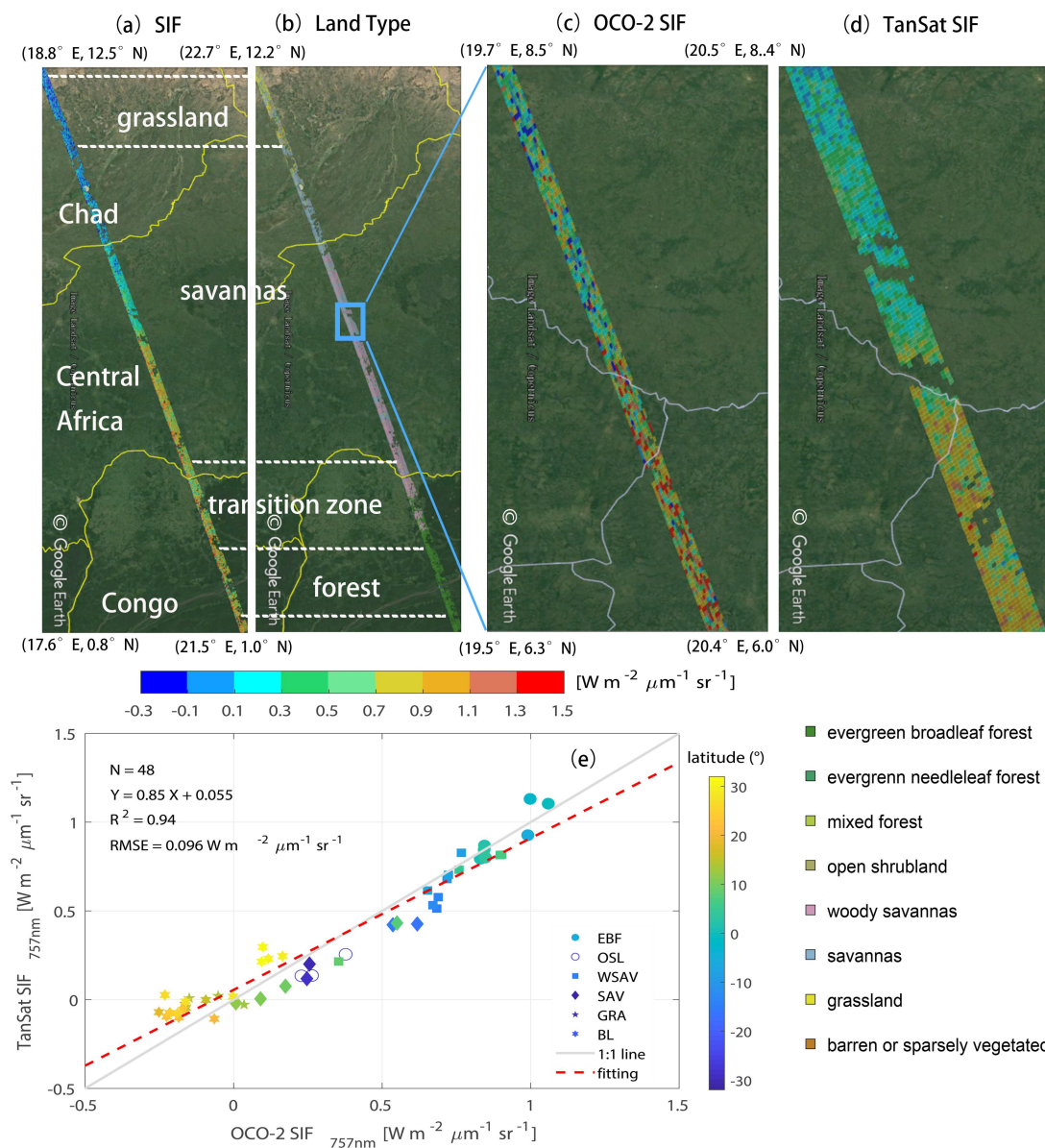
### 204 3.1 Comparison between TanSat and OCO-2 SIF Measurements

205 Directly comparing OCO-2 and TanSat SIF measurements could provide information on joint data application at the  
206 sounding scale for further studies. However, an identical sounding overlap is unlikely because the two satellites have  
207 different nadir tracks on the ground, which means that the orbits normally remain temporal and spatial interval. Fortunately,  
208 the ground tracks of the two satellites were relatively close from April 17 to April 23, 2017. A couple of overlapping orbits  
209 were found in the measurements obtained from Africa with the orbit number of 1733 from TanSat and 14890a from OCO-2  
210 (Figure 3). These overlapping measurements encompassed multiple land cover types, in which the SIF varied within an  
211 acceptable time difference (<5 min).

212 Overall, measurements from the two satellites indicated SIF variation with land cover type. The SIF emission over evergreen  
213 broadleaf forests was larger than that over savannas, and grasslands exhibited the lowest SIF emission in April (Figure 3a,b).  
214 The mean SIF emission over evergreen broadleaf forests was approximately  $0.9\text{--}1.1 \text{ W m}^{-2} \mu\text{m}^{-1} \text{ sr}^{-1}$ , whereas those over  
215 savannas and grasslands were  $0.5\text{--}0.7 \text{ W m}^{-2} \mu\text{m}^{-1} \text{ sr}^{-1}$  and less than  $0.1 \text{ W m}^{-2} \mu\text{m}^{-1} \text{ sr}^{-1}$ , respectively (Figure 3c,d).  
216 Furthermore, we also found a significant difference in the SIF emission intensity over tropical savannas, which was observed  
217 by both satellites (Figure 3c,d).

218





219

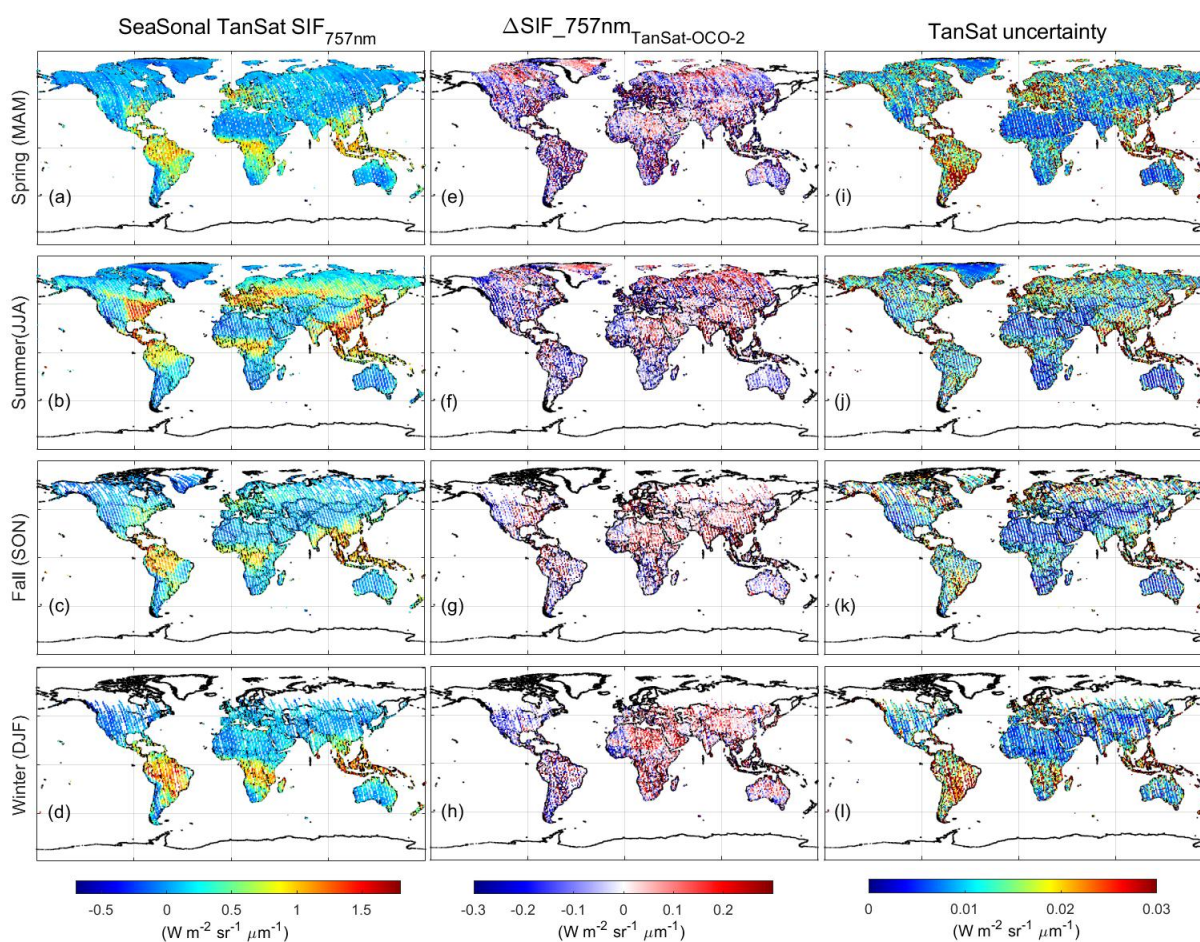
220 Figure 3: Overlapping orbits of TanSat and OCO-2 on April 19, 2017 over Africa displayed in Google Earth, (a) the SIF  
 221 measurements of the two satellites and (b) the footprint land cover type were compared. Compared to OCO-2, TanSat has a wider  
 222 swath width. A zoom-in view over savannas shows variations in the SIF signal measured by (c) OCO-2 and (d) TanSat. The land  
 223 surface image shown in Google Earth is provided by Landsat/Copernicus team. The vertical legend on the bottom right corner  
 224 depicts the land cover type occurs in the study area following the International Geosphere-Biosphere Programme  
 225 scheme, and the middle horizontal color bar represents the intensity of the SIF radiance. (e) Small-area SIF comparison between  
 226 OCO-2 and TanSat; each data point represents the mean SIF of a degree in latitude (colors) along the track. The marker legend  
 227 that is shown on the bottom right of the plot indicates the dominant land cover (defined as the majority land cover type of each  
 228 sounding) in each small area. There are six land cover types including evergreen broadleaf forest (EBF), open shrubland (OSL),  
 229 woody savanna (WSAV), savanna (SAV), grassland (GRA), and barren land (BL). The red dashed line represents the linear fit  
 230 between the two SIF products with statistics shown in the upper left of the plot. The gray line indicates a 1:1 relationship for  
 231 reference.



232

233 Because the footprint sizes of the two satellites are different, it is difficult to make a direct footprint-to-footprint comparison.  
234 Therefore, we made the comparison between the two satellite measurements based on a small area average. Each small area  
235 spans a degree in latitude and continues along the track. The small area-averaged SIF comparison is shown in Figure 3e. The  
236 results indicate good agreement, with an  $R^2$  of 0.94 and an RMSE of  $0.096 \text{ W m}^{-2} \mu\text{m}^{-1} \text{ sr}^{-1}$ . Additional ground-based SIF  
237 measurement setups (Guanter et al., 2007; Liu et al., 2019; van der Tol et al., 2016; Yang et al., 2015a; Yu et al., 2019)  
238 should allow for direct evaluation of satellite retrieval accuracy in the future.

239



240

241 **Figure 4: Global TanSat SIF (left, a-d), differences between TanSat and IAPCAS OCO-2 SIF values (middle, e-h), and the grid-**  
242 **cell retrieval uncertainty estimated from TanSat (right, i-l) at  $1^\circ \times 1^\circ$  spatial resolution. The maps in each row represent a**  
243 **Northern Hemisphere season, i.e., spring (MAM), summer (JJA), fall (SON), and winter (DJF).**

244



245 Figure 4 shows the global SIF comparison between OCO-2 and TanSat; this comparison is only performed at  $1^\circ \times 1^\circ$  spatial  
246 resolution. In general, the difference in SIF globally is mostly less than  $0.3 \text{ W m}^{-2} \mu\text{m}^{-1} \text{ sr}^{-1}$  for all seasons, and on average,  
247 the smallest difference appears in fall. There are regional biases observed in North Africa, South Africa, South America, and  
248 Europe in all seasons except fall. This is mainly caused by the differences in instrument performance between TanSat and  
249 OCO-2, as well as bias corrections. The bias correction compensates for most of the bias caused by instrument performance;  
250 however, small biases could remain. Furthermore, the hundreds of kilometers of distance between the OCO-2 and TanSat  
251 footprints, for example, over different vegetation regions, will also cause some measurement discrepancies.  
252 The uncertainty  $\sigma$  of each sounding was estimated to validate SIF reliability and is provided in the product.  $\sigma$  is derived from  
253 the retrieval error covariance matrix,  $S_e = (K^T S_0^{-1} K)^{-1}$ , where  $K$  is the Jacobian matrix from the forward model fitting and  
254  $S_0$  is the measurement error covariance matrix that is calculated from the instrument spectrum noise. In general,  $\sigma$  ranges  
255 from 0.1 to  $0.6 \text{ W m}^{-2} \mu\text{m}^{-1} \text{ sr}^{-1}$  for both TanSat and OCO-2 measurements in the 757 nm fitting window, which is of a  
256 similar magnitude and data range as those of previous studies (Du et al., 2018; Frankenberg et al., 2014). Meanwhile, the  
257 retrieval uncertainty  $\sigma_{meas}$  of each grid was estimated from TanSat SIF values with  $\sigma_{meas} = \frac{\sigma_{std}}{\sqrt{n}}$  and  $\sigma_{std} = \sqrt{\frac{\sum_{i=1}^n (SIF_i - \overline{SIF})^2}{n}}$ ,  
258 where  $\sigma_{std}$  represents the standard deviation of the grid cell with  $n$  soundings,  $SIF_i$  is the retrieved SIF values of each  
259 sounding, and  $\overline{SIF}$  is the mean SIF value for all measurements in the grid. As depicted in the right column of Figure 4, the  
260  $\sigma_{meas}$  of each grid cell is much lower than the precision of a single sounding. The retrieval uncertainty for South America is  
261 larger than that for any other region on the globe (Figure 4i-l). This is similar to that of OCO-2 SIF retrieval and caused by  
262 fewer effective measurements due to the South Atlantic Anomaly (Sun et al., 2018). The difference in SIF emission values  
263 between the two satellites indicates that the collaborative usage of two satellite SIF products still requires analysis of the  
264 impact of instrument differences, although the two satellite SIF products share the same spatiotemporal pattern on a global  
265 scale.

### 266 3.2 SIF Global Distribution and Temporal Variation

267 The SIF emission intensity reflects the growth status of vegetation due to its correlation with photosynthetic efficiency;  
268 hence, the overall global vegetation status can be represented by global SIF maps for each season. TanSat SIF over a whole  
269 year's cycle, from March 2017 to February 2018, is represented seasonally as a  $1^\circ \times 1^\circ$  grid spatially. The seasonal variation  
270 in SIF emission is clear in the Northern Hemisphere, i.e., it is enhanced from spring to summer and then decreases (Sun et al.,  
271 2018).

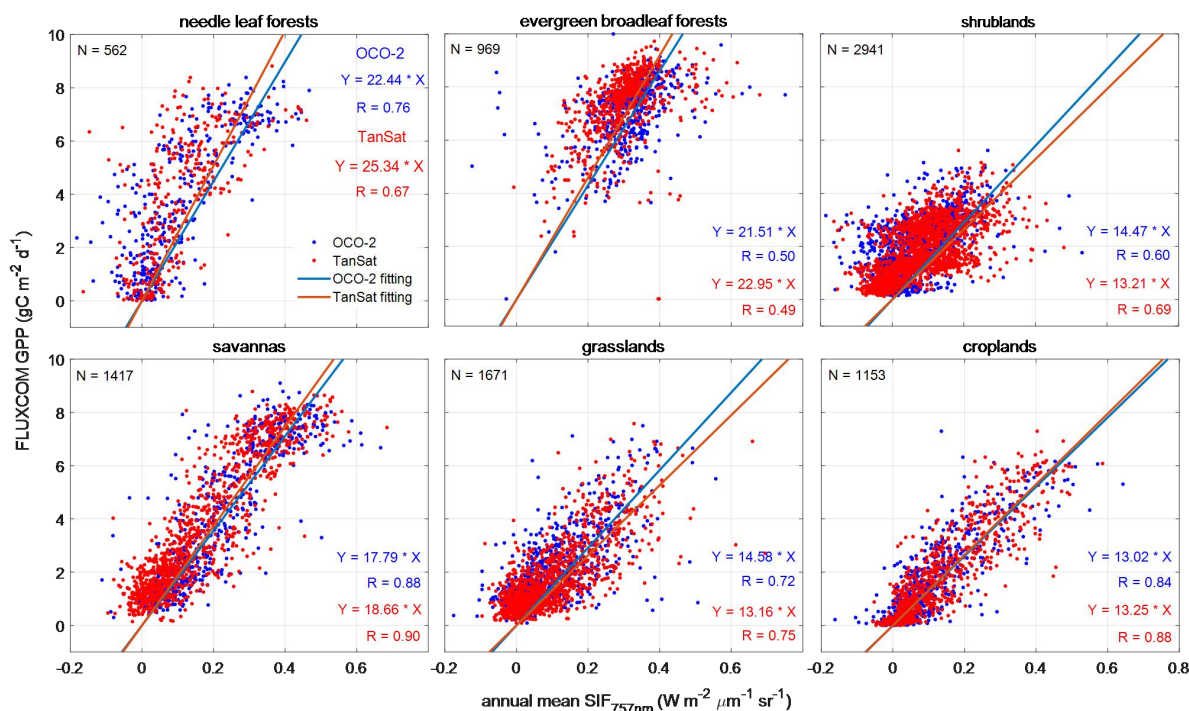
272 In general, the SIF emission varied with latitude and the vegetation-covered areas near the equator maintained a continuous  
273 SIF emission throughout the year. Large SIF emissions in the Northern Hemisphere, above  $1.5 \text{ W m}^{-2} \mu\text{m}^{-1} \text{ sr}^{-1}$ , mostly from  
274 the eastern U.S., southeast of China, and southern Asia in summer, were due to the large areas of cropland. There was also  
275 an obvious SIF emission of  $1\text{-}1.2 \text{ W m}^{-2} \mu\text{m}^{-1} \text{ sr}^{-1}$  observed over Central Europe and northeastern China during the summer.  
276 In these regions, croplands and deciduous forests contribute to SIF emissions. In the Southern Hemisphere, the strongest SIF



277 emission occurred in the Amazon, with a level of approximately  $1\text{-}2 \text{ W m}^{-2} \mu\text{m}^{-1} \text{ sr}^{-1}$  in DJF (Northern Hemisphere winter),  
 278 where there is an evergreen broadleaf rainforest. Africa, which is covered by evergreen broadleaf rainforests and woody  
 279 savannas, had an average SIF value of  $0.7\text{-}1.5 \text{ W m}^{-2} \mu\text{m}^{-1} \text{ sr}^{-1}$  during the year.  
 280 The SIF-GPP relationship over different vegetation types was also investigated by comparing the annual mean satellite SIF  
 281 measurements with the FLUXCOM GPP (Jung et al., 2020; Tramontana et al., 2016) dataset in a  $1^\circ \times 1^\circ$  grid over the globe.  
 282 The FLUXCOM GPP dataset used in the study comprises monthly global gridded flux products with remote sensing and  
 283 meteorological/climate forcing (RS+METEO) setups, which are derived from mean seasonal cycles according to MODIS  
 284 data and daily meteorological information (Jung et al., 2020; Tramontana et al., 2016). The satellite-measured SIF is an  
 285 instantaneous emission signal that varies with incident solar radiance within the day. To reduce the differences caused by the  
 286 observation time and SZA at different latitudes, we applied a daily adjustment factor to convert the instantaneous SIF  
 287 emission into a daily mean SIF (Du et al., 2018; Frankenberg et al., 2011b; Sun et al., 2018). The daily adjustment factor  $d$  is  
 288 calculated as follows:

$$289 \quad d = \frac{\int_{t=t_0-12h}^{t=t_0+12h} \cos(SZA(t)) \cdot dt}{\cos(SZA(t_0))} \quad (5)$$

290 where  $t_0$  is the observation time in fractional days and  $SZA(t)$  is a function of latitude, longitude, and time for calculating  
 291 the SZA of the measurements. The annual averaged SIF is calculated from the daily mean SIF. To evaluate the relationship  
 292 between SIF and GPP on the periodic scale of vegetation growth status, annually-averaged data were used in the regression  
 293 fitting analysis.



294



295 **Figure 5: Relationship between annual mean SIF and FLUXCOM gross primary production (GPP) from March 2017 to February**  
296 **2018. Red and blue dots represent OCO-2 and TanSat SIF grids, respectively. Fitted lines and statistics for OCO-2 and TanSat are**  
297 **shown in each plot.**

298 Figure 5 shows the linear fits for six vegetation types, including needle leaf forest, evergreen broadleaf forest, shrubland,  
299 savanna, grassland, and cropland. Recent studies have shown a strong linear correlation between SIF and GPP. To make a  
300 direct comparison of the relationship between SIF and GPP among various vegetation types, we used non-offset linear fitting  
301 to indicate the correlation between satellite SIF and FLUXCOM GPP. For savanna and cropland, there were strong  
302 relationships between the mean SIF and GPP with an R-value above 0.84. The fitting results show that the SIF products of  
303 the two satellites have similar capabilities in characterizing GPP, especially for the evergreen broadleaf forest, savanna, and  
304 cropland, with slopes of approximately 21, 18, and 13, respectively. The markedly different fitting slopes across various  
305 biomes suggest that the application of SIF in GPP estimation needs more detailed analysis although the evidence of the  
306 strong linear relationship between them.

#### 307 **4 Conclusions**

308 In this paper, we introduced the retrieval algorithm IAPCAS/SIF and its application in TanSat and OCO-2 measurements.  
309 One-year (March 2017-February 2018) TanSat SIF data was introduced and compared with OCO-2 measurements in this  
310 study. The TanSat and OCO-2 SIF products based on the IAPCAS/SIF algorithm are available on the Cooperation on the  
311 Analysis of carbon SATellites data (CASA) website, [www.chinageoss.org/tansat](http://www.chinageoss.org/tansat). Comparisons between TanSat and OCO-2  
312 measurements directly, using a case study, and indirectly, with global  $1^{\circ} \times 1^{\circ}$  grid data, showed consistency between the two  
313 satellite missions, indicating that the coordinated usage of the two data products is possible in future studies. With increasing  
314 satellites becoming available for SIF observations, space-based SIF observations have recently expanded in range to provide  
315 broad spatiotemporal coverage. The next-generation Chinese carbon monitoring satellite (TanSat-2) is now in the  
316 preliminary design phase. SIF measurements from TanSat-2 will provide global data products over broader coverage areas  
317 with less noise. The improvement in the spatiotemporal resolution of SIF data will benefit GPP predictions based on the  
318 numerous studies of the linear relationship between SIF and GPP. In future work, the measurement accuracy should be  
319 validated directly using ground-based measurements to ensure data quality.

#### 320 **Data availability**

321 The SIF products of TanSat and OCO-2 by IAPCAS/SIF algorithm are available on the Cooperation on the Analysis of  
322 carbon SATellites data (CASA) website ([www.chinageoss.org/tansat](http://www.chinageoss.org/tansat)).

323



### 324 **Author contributions**

325 L.Y. and D.Y. developed the retrieval algorithm, designed the study, and wrote the paper. Y.L. led the SIF data process and  
326 analysis. Y.L., D.Y., Z.C., and J.W. contributed to manuscript organization and revision. C.L. and Y.Z. provided information  
327 on the TanSat instrument performance. L.T. provided TanSat in-flight information. M.W. and S.W. provided information on  
328 the scientific requirement for data further application. N.L. and D.L. led the TanSat data application. Z.Y. led the TanSat in-  
329 flight operation.

### 330 **Competing interests**

331 The authors declare that they have no conflict of interest.

### 332 **Acknowledgments**

333 The TanSat L1B data service was provided by the International Reanalysis Cooperation on Carbon Satellites Data (IRCSD)  
334 and the Cooperation on the Analysis of carbon Satellites data (CASA). The authors thank OCO-2 Team for providing  
335 Level-1B data and Level-2 SIF data products. The authors thank the FLUXCOM team for providing global GPP data. The  
336 authors thank Google for allowing free use of Google Earth and reproduction of maps for publication. The authors also thank  
337 the Landsat/Copernicus team for providing land surface images for Google Earth.

### 338 **Financial support**

339 This work has been supported by the National Key R&D Program of China (No. 2016YFA0600203), The Key Research  
340 Program of the Chinese Academy of Sciences (ZDRW-ZS-2019-1), and the Youth Program of the National Natural Science  
341 Foundation of China (41905029).

### 342 **References**

- 343 Boesche, E., Stammes, P., and Bennartz, R.: Aerosol influence on polarization and intensity in near-infrared O<sub>2</sub> and CO<sub>2</sub>  
344 absorption bands observed from space, *J. Quant. Spectrosc. Radiat. Transf.*, 110, 223–239,  
345 <https://doi.org/10.1016/j.jqsrt.2008.09.019>, 2009.
- 346 Butz, A., Guerlet, S., Hasekamp, O., Schepers, D., Galli, A., Aben, I., Frankenberg, C., Hartmann, J. M., Tran, H., Kuze, A.,  
347 Keppel-Aleks, G., Toon, G., Wunch, D., Wennberg, P., Deutscher, N., Griffith, D., Macatangay, R., Messerschmidt, J.,  
348 Notholt, J., and Warneke, T.: Toward accurate CO<sub>2</sub> and CH<sub>4</sub> observations from GOSAT, *Geophys. Res. Lett.*, 38, 2–7,  
349 <https://doi.org/10.1029/2011GL047888>, 2011.



- 350 Butz, A., Hasekamp, O. P., Frankenberg, C., and Aben, U.: Retrievals of atmospheric CO<sub>2</sub> from simulated space-borne  
351 measurements of backscattered near-infrared sunlight: Accounting for aerosol effects, *Appl. Opt.*, 48, 3322–3336,  
352 <https://doi.org/10.1364/AO.48.003322>, 2009.
- 353 Butz, A., Hasekamp, O. P., Frankenberg, C., Vidot, J., and Aben, I.: CH<sub>4</sub> retrievals from space-based solar backscatter  
354 measurements: Performance evaluation against simulated aerosol and cirrus loaded scenes, *J. Geophys. Res. Atmos.*, 115, 1–  
355 15, <https://doi.org/10.1029/2010JD014514>, 2010.
- 356 Cai, Z. N., Liu, Y., and Yang, D. X.: Analysis of XCO<sub>2</sub> retrieval sensitivity using simulated Chinese Carbon Satellite  
357 (TanSat) measurements, *Sci. China Earth Sci.*, 57, 1919–1928, <https://doi.org/10.1007/s11430-013-4707-1>, 2014.
- 358 Chen, A., Mao, J., Ricciuto, D., Xiao, J., Frankenberg, C., Li, X., Thornton, P. E., Gu, L., and Knapp, A. K.: Moisture  
359 availability mediates the relationship between terrestrial gross primary production and solar-induced chlorophyll  
360 fluorescence: Insights from global-scale variations, *Glob. Chang. Biol.*, 1–13, <https://doi.org/10.1111/gcb.15373>, 2020.
- 361 Doughty, R., Köhler, P., Frankenberg, C., Magney, T. S., Xiao, X., Qin, Y., Wu, X., and Moore, B.: TROPOMI reveals dry-  
362 season increase of solar-induced chlorophyll fluorescence in the Amazon forest, *Proc. Natl. Acad. Sci. U. S. A.*, 116, 22393–  
363 22398, <https://doi.org/10.1073/pnas.1908157116>, 2019.
- 364 Drusch, M., Moreno, J., del Bello, U., Franco, R., Goulas, Y., Huth, A., Kraft, S., Middleton, E. M., Miglietta, F.,  
365 Mohammed, G.: The FLuorescence EXplorer Mission Concept—ESA’s Earth Explorer 8, *ITGRS*, 55, 1273–1284,  
366 <http://doi.org/10.1109/TGRS.2016.2621820>, 2017.
- 367 Du, S., Liu, L., Liu, X., Zhang, X., Zhang, X., Bi, Y., and Zhang, L.: Retrieval of global terrestrial solar-induced chlorophyll  
368 fluorescence from TanSat satellite, *Sci. Bull.*, 63, 1502–1512, <https://doi.org/10.1016/j.scib.2018.10.003>, 2018.
- 369 Frankenberg, C., Butz, A., and Toon, G. C.: Disentangling chlorophyll fluorescence from atmospheric scattering effects in  
370 O<sub>2</sub> A-band spectra of reflected sunlight, *Geophys. Res. Lett.*, 38, 1–5, <https://doi.org/10.1029/2010GL045896>, 2011a.
- 371 Frankenberg, C., Fisher, J. B., Worden, J., Badgley, G., Saatchi, S. S., Lee, J. E., Toon, G. C., Butz, A., Jung, M., Kuze, A.,  
372 and Yokota, T.: New global observations of the terrestrial carbon cycle from GOSAT: Patterns of plant fluorescence with  
373 gross primary productivity, *Geophys. Res. Lett.*, 38, 1–6, <https://doi.org/10.1029/2011GL048738>, 2011b.
- 374 Frankenberg, C., O’Dell, C., Berry, J., Guanter, L., Joiner, J., Köhler, P., Pollock, R., and Taylor, T. E.: Prospects for  
375 chlorophyll fluorescence remote sensing from the Orbiting Carbon Observatory-2, *Remote Sens. Environ.*, 147, 1–12,  
376 <https://doi.org/10.1016/j.rse.2014.02.007>, 2014.
- 377 Frankenberg, C., O’Dell, C., Guanter, L., and McDuffie, J.: Remote sensing of near-infrared chlorophyll fluorescence from  
378 space in scattering atmospheres: Implications for its retrieval and interferences with atmospheric CO<sub>2</sub> retrievals, *Atmos.*  
379 *Meas. Tech.*, 5, 2081–2094, <https://doi.org/10.5194/amt-5-2081-2012>, 2012.
- 380 Guanter, L., Aben, I., Tol, P., Krijger, J. M., Hollstein, A., Köhler, P., Damm, A., Joiner, J., Frankenberg, C., and Landgraf,  
381 J.: Potential of the TROPOspheric Monitoring Instrument (TROPOMI) onboard the Sentinel-5 Precursor for the monitoring  
382 of terrestrial chlorophyll fluorescence, <https://doi.org/10.5194/amt-8-1337-2015>, 2015.



- 383 Guanter, L., Alonso, L., Gómez-Chova, L., Amorós-López, J., Vila, J., and Moreno, J.: Estimation of solar-induced  
384 vegetation fluorescence from space measurements, *Geophys. Res. Lett.*, 34, 1–5, <https://doi.org/10.1029/2007GL029289>,  
385 2007.
- 386 Guanter, L., Frankenberg, C., Dudhia, A., Lewis, P. E., Gómez-Dans, J., Kuze, A., Suto, H., and Grainger, R. G.: Retrieval  
387 and global assessment of terrestrial chlorophyll fluorescence from GOSAT space measurements, *Remote Sens. Environ.*, 121,  
388 236–251, <https://doi.org/10.1016/j.rse.2012.02.006>, 2012.
- 389 Guanter, L., Zhang, Y., Jung, M., Joiner, J., Voigt, M., Berry, J. A., Frankenberg, C., Huete, A. R., Zarco-Tejada, P., Lee, J.  
390 E., Moran, M. S., Ponce-Campos, G., Beer, C., Camps-Valls, G., Buchmann, N., Gianelle, D., Klumpp, K., Cescatti, A.,  
391 Baker, J. M., and Griffis, T. J.: Global and time-resolved monitoring of crop photosynthesis with chlorophyll fluorescence,  
392 *Proc. Natl. Acad. Sci. U. S. A.*, 111, <https://doi.org/10.1073/pnas.1320008111>, 2014.
- 393 Joiner, J., Guanter, L., Lindstrot, R., Voigt, M., Vasilkov, A. P., Middleton, E. M., Huemmrich, K. F., Yoshida, Y., and  
394 Frankenberg, C.: Global monitoring of terrestrial chlorophyll fluorescence from moderate-spectral-resolution near-infrared  
395 satellite measurements: methodology, simulations, and application to GOME-2, *Atmos. Meas. Tech.*, 6, 2803–2823,  
396 <https://doi.org/10.5194/amt-6-2803-2013>, 2013.
- 397 Joiner, J., Yoshida, Y., Guanter, L., and Middleton, E. M.: New methods for the retrieval of chlorophyll red fluorescence  
398 from hyperspectral satellite instruments: simulations and application to GOME-2 and SCIAMACHY, *Atmos. Meas. Tech.*, 9,  
399 3939–3967, <https://doi.org/10.5194/amt-9-3939-2016>, 2016.
- 400 Joiner, J., Yoshida, Y., Vasilkov, A. P., Middleton, E. M., Campbell, P. K. E., Yoshida, Y., Kuze, A., and Corp, L. A.:  
401 Filling-in of near-infrared solar lines by terrestrial fluorescence and other geophysical effects: simulations and space-based  
402 observations from SCIAMACHY and GOSAT, *Atmos. Meas. Tech.*, 5, 809–829, <https://doi.org/10.5194/amt-5-809-2012>,  
403 2012.
- 404 Joiner, J., Yoshida, Y., Vasilkov, A. P., Yoshida, Y., Corp, L. A., and Middleton, E. M.: First observations of global and  
405 seasonal terrestrial chlorophyll fluorescence from space, 8, 637–651, <https://doi.org/10.5194/bg-8-637-2011>, 2011.
- 406 Joiner, J., Yoshida, Y., Zhang, Y., Duveiller, G., Jung, M., Lyapustin, A., Wang, Y., and Tucker, C. J.: Estimation of  
407 terrestrial global gross primary production (GPP) with satellite data-driven models and eddy covariance flux data, *Remote*  
408 *Sens.*, 10, 1–38, <https://doi.org/10.3390/rs10091346>, 2018.
- 409 Jung, M., Schwalm, C., Migliavacca, M., Walther, S., Camps-Valls, G., Koirala, S., Anthoni, P., Besnard, S., Bodesheim, P.,  
410 Carvalhais, N., Chevallier, F., Gans, F., S Goll, D., Haverd, V., Köhler, P., Ichii, K., K Jain, A., Liu, J., Lombardozzi, D., E  
411 M S Nabel, J., A Nelson, J., O’Sullivan, M., Pallandt, M., Papale, D., Peters, W., Pongratz, J., Rödenbeck, C., Sitch, S.,  
412 Tramontana, G., Walker, A., Weber, U., and Reichstein, M.: Scaling carbon fluxes from eddy covariance sites to globe:  
413 Synthesis and evaluation of the FLUXCOM approach, 17, 1343–1365, <https://doi.org/10.5194/bg-17-1343-2020>, 2020.
- 414 Köhler, P., Frankenberg, C., Magney, T. S., Guanter, L., Joiner, J., and Landgraf, J.: Global Retrievals of Solar-Induced  
415 Chlorophyll Fluorescence With TROPOMI: First Results and Intersensor Comparison to OCO-2, *Geophys. Res. Lett.*, 45,  
416 10,456-10,463, <https://doi.org/10.1029/2018GL079031>, 2018b.





- 417 Köhler, P., Guanter, L., and Joiner, J.: A linear method for the retrieval of sun-induced chlorophyll fluorescence from  
418 GOME-2 and SCIAMACHY data, *Atmos. Meas. Tech.*, 8, 2589–2608, <https://doi.org/10.5194/amt-8-2589-2015>, 2015.
- 419 Köhler, P., Guanter, L., Kobayashi, H., Walther, S., and Yang, W.: Assessing the potential of sun-induced fluorescence and  
420 the canopy scattering coefficient to track large-scale vegetation dynamics in Amazon forests, *Remote Sens. Environ.*, 204,  
421 769–785, <https://doi.org/10.1016/j.rse.2017.09.025>, 2018a.
- 422 Lee, J. E., Frankenberg, C., Van Der Tol, C., Berry, J. A., Guanter, L., Boyce, C. K., Fisher, J. B., Morrow, E., Worden, J. R.,  
423 Asefi, S., Badgley, G., and Saatchi, S.: Forest productivity and water stress in Amazonia: Observations from GOSAT  
424 chlorophyll fluorescence, *Tohoku J. Exp. Med.*, 230, <https://doi.org/10.1098/rspb.2013.0171>, 2013.
- 425 Li, X., Xiao, J., and He, B.: Chlorophyll fluorescence observed by OCO-2 is strongly related to gross primary productivity  
426 estimated from flux towers in temperate forests, *Remote Sens. Environ.*, 204, 659–671,  
427 <https://doi.org/10.1016/j.rse.2017.09.034>, 2018.
- 428 Li, X., Xiao, J., Kimball, J. S., Reichle, R. H., Scott, R. L., Litvak, M. E., Bohrer, G., and Frankenberg, C.: Synergistic use of  
429 SMAP and OCO-2 data in assessing the responses of ecosystem productivity to the 2018 U.S. drought, *Remote Sens.*  
430 *Environ.*, 251, 112062, <https://doi.org/10.1016/j.rse.2020.112062>, 2020.
- 431 Liu, X., Guanter, L., Liu, L., Damm, A., Malenovský, Z., Rascher, U., Peng, D., Du, S., and Gastellu-Etchegorry, J. P.:  
432 Downscaling of solar-induced chlorophyll fluorescence from canopy level to photosystem level using a random forest model,  
433 *Remote Sens. Environ.*, 231, 110772, <https://doi.org/10.1016/j.rse.2018.05.035>, 2019.
- 434 Liu, Y., Wang, J., Yao, L., Chen, X., Cai, Z., Yang, D., Yin, Z., Gu, S., Tian, L., Lu, N., and Lyu, D.: The TanSat mission:  
435 preliminary global observations, *Sci. Bull.*, 63, 1200–1207, <https://doi.org/10.1016/j.scib.2018.08.004>, 2018.
- 436 MacBean, N., Maignan, F., Bacour, C., Lewis, P., Peylin, P., Guanter, L., Köhler, P., Gómez-Dans, J., and Disney, M.:  
437 Strong constraint on modelled global carbon uptake using solar-induced chlorophyll fluorescence data, *Sci. Rep.*, 8, 1–12,  
438 <https://doi.org/10.1038/s41598-018-20024-w>, 2018.
- 439 O’Dell, C. W., Connor, B., Bösch, H., O’Brien, D., Frankenberg, C., Castano, R., Christi, M., Eldering, D., Fisher, B.,  
440 Gunson, M., McDuffie, J., Miller, C. E., Natraj, V., Oyafuso, F., Polonsky, I., Smyth, M., Taylor, T., Toon, G. C., Wennberg,  
441 P. O., and Wunch, D.: The ACOS CO<sub>2</sub> retrieval algorithm-Part 1: Description and validation against synthetic observations,  
442 *Atmos. Meas. Tech.*, 5, 99–121, <https://doi.org/10.5194/amt-5-99-2012>, 2012.
- 443 Qiu, R., Han, G., Ma, X., Xu, H., Shi, T., and Zhang, M.: A comparison of OCO-2 SIF, MODIS GPP, and GOSIF data from  
444 gross primary production (GPP) estimation and seasonal cycles in North America, *Remote Sens.*, 12,  
445 <https://doi.org/10.3390/rs12020258>, 2020.
- 446 Reuter, M., Buchwitz, M., Schneising, O., Heymann, J., Bovensmann, H., and Burrows, J. P.: A method for improved  
447 SCIAMACHY CO<sub>2</sub> retrieval in the presence of optically thin clouds, *Atmos. Meas. Tech.*, 3, 209–232,  
448 <https://doi.org/10.5194/amt-3-209-2010>, 2010.



- 449 Sun, K., Liu, X., Nowlan, C. R., Cai, Z., Chance, K., Frankenberg, C., Lee, R. A. M., Pollock, R., Rosenberg, R., and Crisp,  
450 D.: Characterization of the OCO-2 instrument line shape functions using on-orbit solar measurements, *Atmos. Meas. Tech.*,  
451 10, 939–953, <https://doi.org/10.5194/amt-10-939-2017>, 2017b.
- 452 Sun, Y., Frankenberg, C., Jung, M., Joiner, J., Guanter, L., Köhler, P., and Magney, T.: Overview of Solar-Induced  
453 chlorophyll Fluorescence (SIF) from the Orbiting Carbon Observatory-2: Retrieval, cross-mission comparison, and global  
454 monitoring for GPP, *Remote Sens. Environ.*, 209, 808–823, <https://doi.org/10.1016/j.rse.2018.02.016>, 2018.
- 455 Sun, Y., Frankenberg, C., Wood, J. D., Schimel, D. S., Jung, M., Guanter, L., Drewry, D. T., Verma, M., Porcar-Castell, A.,  
456 Griffiths, T. J., Gu, L., Magney, T. S., Köhler, P., Evans, B., and Yuen, K.: OCO-2 advances photosynthesis observation from  
457 space via solar-induced chlorophyll fluorescence, *Science (80-. )*, 358, <https://doi.org/10.1126/science.aam5747>, 2017a.
- 458 Sun, Y., Fu, R., Dickinson, R., Joiner, J., Frankenberg, C., Gu, L., Xia, Y., and Fernando, N.: Drought onset mechanisms  
459 revealed by satellite solar-induced chlorophyll fluorescence: Insights from two contrasting extreme events, *J. Geophys. Res.*  
460 *G Biogeosciences*, 120, 2427–2440, <https://doi.org/10.1002/2015JG003150>, 2015.
- 461 Tramontana, G., Jung, M., Schwalm, C. R., Ichii, K., Camps-Valls, G., Ráduly, B., Reichstein, M., Arain, M. A., Cescatti, A.,  
462 Kiely, G., Merbold, L., Serrano-Ortiz, P., Sickert, S., Wolf, S., and Papale, D.: Predicting carbon dioxide and energy fluxes  
463 across global FLUXNET sites with regression algorithms, 13, 4291–4313, <https://doi.org/10.5194/bg-13-4291-2016>, 2016.
- 464 van der Tol, C., Rossini, M., Cogliati, S., Verhoef, W., Colombo, R., Rascher, U., and Mohammed, G.: A model and  
465 measurement comparison of diurnal cycles of sun-induced chlorophyll fluorescence of crops, *Remote Sens. Environ.*, 186,  
466 663–677, <https://doi.org/10.1016/j.rse.2016.09.021>, 2016.
- 467 Yang, D., Boesch, H., Liu, Y., Somkuti, P., Cai, Z., Chen, X., Di Noia, A., Lin, C., Lu, N., Lyu, D., Parker, R. J., Tian, L.,  
468 Wang, M., Webb, A., Yao, L., Yin, Z., Zheng, Y., Deutscher, N. M., Griffith, D. W. T., Hase, F., Kivi, R., Morino, I.,  
469 Notholt, J., Ohyama, H., Pollard, D. F., Shiomi, K., Sussmann, R., Té, Y., Velazco, V. A., Warneke, T., and Wunch, D.:  
470 Toward High Precision XCO<sub>2</sub> Retrievals From TanSat Observations: Retrieval Improvement and Validation Against  
471 TCCON Measurements, *J. Geophys. Res. Atmos.*, 125, 1–26, <https://doi.org/10.1029/2020JD032794>, 2020.
- 472 Yang, D., Liu, Y., Boesch, H., Yao, L., Di Noia, A., Cai, Z., Lu, N., Lyu, D., Wang, M., Wang, J., Yin, Z., and Zheng, Y.: A  
473 New TanSat XCO<sub>2</sub> Global Product towards Climate Studies, *Adv. Atmos. Sci.*, 38, 8–11, [https://doi.org/10.1007/s00376-](https://doi.org/10.1007/s00376-020-0297-y)  
474 [020-0297-y](https://doi.org/10.1007/s00376-020-0297-y), 2021.
- 475 Yang, D., Liu, Y., Cai, Z., Chen, X., Yao, L., and Lu, D.: First Global Carbon Dioxide Maps Produced from TanSat  
476 Measurements, *Adv. Atmos. Sci.*, 35, 621–623, <https://doi.org/10.1007/s00376-018-7312-6>, 2018.
- 477 Yang, D., Liu, Y., Cai, Z., Deng, J., Wang, J., and Chen, X.: An advanced carbon dioxide retrieval algorithm for satellite  
478 measurements and its application to GOSAT observations, *Sci. Bull.*, 60, 2063–2066, [https://doi.org/10.1007/s11434-015-](https://doi.org/10.1007/s11434-015-0953-2)  
479 [0953-2](https://doi.org/10.1007/s11434-015-0953-2), 2015b.
- 480 Yang, X., Tang, J., Mustard, J. F., Lee, J. E., Rossini, M., Joiner, J., Munger, J. W., Kornfeld, A., and Richardson, A. D.:  
481 Solar-induced chlorophyll fluorescence that correlates with canopy photosynthesis on diurnal and seasonal scales in a  
482 temperate deciduous forest, *Geophys. Res. Lett.*, 42, 2977–2987, <https://doi.org/10.1002/2015GL063201>, 2015a.



- 483 Yao, L., Yang, D., Liu, Y., Wang, J., Liu, L., Du, S., Cai, Z., Lu, N., Lyu, D., Wang, M., Yin, Z., and Zheng, Y.: A New  
484 Global Solar-induced Chlorophyll Fluorescence (SIF) Data Product from TanSat Measurements, *Adv. Atmos. Sci.*, 38, 341–  
485 345, <https://doi.org/10.1007/s00376-020-0204-6>, 2021.
- 486 Yin, Y., Byrne, B., Liu, J., Wennberg, P. O., Davis, K. J., Magney, T., Köhler, P., He, L., Jeyaram, R., Humphrey, V.,  
487 Gerken, T., Feng, S., Digangi, J. P., and Frankenberg, C.: Cropland Carbon Uptake Delayed and Reduced by 2019 Midwest  
488 Floods, *AGU Adv.*, 1, 1–15, <https://doi.org/10.1029/2019av000140>, 2020.
- 489 Yoshida, Y., Joiner, J., Tucker, C., Berry, J., Lee, J. E., Walker, G., Reichle, R., Koster, R., Lyapustin, A., and Wang, Y.:  
490 The 2010 Russian drought impact on satellite measurements of solar-induced chlorophyll fluorescence: Insights from  
491 modeling and comparisons with parameters derived from satellite reflectances, *Remote Sens. Environ.*, 166, 163–177,  
492 <https://doi.org/10.1016/j.rse.2015.06.008>, 2015.
- 493 Yoshida, Y., Kikuchi, N., Morino, I., Uchino, O., Oshchepkov, S., Bril, A., Saeki, T., Schutgens, N., Toon, G. C., Wunch, D.,  
494 Roehl, C. M., Wennberg, P. O., Griffith, D. W. T., Deutscher, N. M., Warneke, T., Notholt, J., Robinson, J., Sherlock, V.,  
495 Connor, B., Rettinger, M., Sussmann, R., Ahonen, P., Heikkinen, P., Kyrö, E., Mendonca, J., Strong, K., Hase, F., Dohe, S.,  
496 and Yokota, T.: Improvement of the retrieval algorithm for GOSAT SWIR XCO<sub>2</sub> and XCH<sub>4</sub> and their validation using  
497 TCCON data, *Atmos. Meas. Tech.*, 6, 1533–1547, <https://doi.org/10.5194/amt-6-1533-2013>, 2013.
- 498 Yoshida, Y., Ota, Y., Eguchi, N., Kikuchi, N., Nobuta, K., Tran, H., Morino, I., and Yokota, T.: Retrieval algorithm for CO<sub>2</sub>  
499 and CH<sub>4</sub> column abundances from short-wavelength infrared spectral observations by the Greenhouse gases observing  
500 satellite, *Atmos. Meas. Tech.*, 4, 717–734, <https://doi.org/10.5194/amt-4-717-2011>, 2011.
- 501 Yu, L., Wen, J., Chang, C. Y., Frankenberg, C., and Sun, Y.: High-Resolution Global Contiguous SIF of OCO-2, *Geophys.*  
502 *Res. Lett.*, 46, 1449–1458, <https://doi.org/10.1029/2018GL081109>, 2019.
- 503 Zhang, Y., Guanter, L., Berry, J. A., Joiner, J., van der Tol, C., Huete, A., Gitelson, A., Voigt, M., and Köhler, P.: Estimation  
504 of vegetation photosynthetic capacity from space-based measurements of chlorophyll fluorescence for terrestrial biosphere  
505 models, *Glob. Chang. Biol.*, 20, 3727–3742, <https://doi.org/10.1111/gcb.12664>, 2014.
- 506 Zhang, Y., Xiao, X., Zhang, Y., Wolf, S., Zhou, S., Joiner, J., Guanter, L., Verma, M., Sun, Y., Yang, X., Paul-Limoges, E.,  
507 Gough, C. M., Wohlfahrt, G., Gioli, B., van der Tol, C., Yann, N., Lund, M., and de Grandcourt, A.: On the relationship  
508 between sub-daily instantaneous and daily total gross primary production: Implications for interpreting satellite-based SIF  
509 retrievals, *Remote Sens. Environ.*, 205, 276–289, <https://doi.org/10.1016/j.rse.2017.12.009>, 2018.

510  
511  
512  
513